Journal of Non-Newtonian Fluid Mechanics, 5 (1979) 323—352
© Elsevier Scientific Publishing Company, Amsterdam — Printed in The Netherlands

EXPERIMENTS ON FREE SURFACE PHENOMENA *

G.S. BEAVERS and D.D. JOSEPH

Department of Aerospace Engineering and Mechanics, University of Minnesota, Minneapolis, Minnesota 55455 (U.S.A.)

(Received July 20, 1978)

Summary

This paper reviews an experimental program in which predictions from domain perturbation theory for motions which perturb the rest state are used in conjunction with experimental measurements on free surface deformations associated with the Weissenberg effect at low rates of shear to obtain values for certain rheological parameters. The experiments include free surface measurements on a liquid near a circular rod rotating in steady motion and oscillatory motion in a large volume of fluid, secondary flows and circumferential velocity measurements in steady rod climbing, normal stress amplification effects, and free surface shapes on a fluid confined between rotating cylinders. Temperature effects are noted, and interesting instability phenomena at high rates of shearing are demonstrated.

1. Introduction

In an earlier paper [1] we reviewed our work on the potential for making rheometrical measurements on viscoelastic fluids from the study of free surface deformations induced by motions which perturb the rest state. The primary emphasis in that review was placed on the theoretical foundations of our work. In particular, an introduction to Joseph's method of domain perturbations was presented, and the application of the method to motions in several simple experimental geometries was demonstrated. The present paper is intended as a companion paper to reference [1]. Here we emphasize the

* Presented at the IUTAM Symposium on Non-Newtonian Fluid Mechanics, Louvain-La-Neuve, Belgium, 28 August—1 September, 1978.

experimental aspects of our work, giving a brief overview of the experimental program and including some results we have obtained since the appearance of the earlier review. The theme of the present paper is to show how important characterizing properties of viscoelastic fluids can be determined through a combination of simple experimental geometry and perturbation analysis. The paper also includes brief descriptions of some interesting phenomena which can arise in flow regimes which are beyond the applicability of the perturbation technique, and which have not yet been subjected to analytical investigation.

Possibly the simplest experimental configuration from which to study free surface phenomena is that associated with the Weissenberg effect, and it is this configuration that has been used for the work described in this paper. The Weissenberg effect is usually described as the climbing of a viscoelastic fluid up the inner rotating cylinder when the fluid is sheared in a Couette motion between concentric rotating cylinders, or as the climbing of a viscoelastic fluid up a circular rod which rotates in a large volume of the fluid. In this paper we extend somewhat the description of the Weissenberg effect to include any type of free surface deformation on a viscoelastic fluid between concentric rotating cylinders, even though the fluid may not climb up the inner cylinder. We present results from several Weissenberg-type experiments. These include the steady rotation and torsional oscillations of circular rods in large volumes of fluid, the steady rotation of circular rods in layered fluids, and the motion of a fluid between concentric rotating cylinders.

2. Steady rod climbing

The experiments described in this section are concerned with a circular rod rotating at constant angular speed in a large volume of viscoelastic fluid. If the radius of the rod is not larger than a certain critical radius the fluid will climb up the rod. This problem has been subjected to several analytical investigations, which are reported in [1].

The perturbation analysis has been completed through order four [2—6]. In the perturbation approach the extra stress $\boldsymbol{S}$ is expanded into a series of Rivlin—Ericksen kinematic tensors A_n such that the partial sum $S_{(N)}$ is given by

$$S_{(N)} = \sum_{1}^{N} S_n[A_n, A_{n-1}, \ldots A_1],$$

where the first four tensors S_n are

$$S_1[A_1] = \mu A_1, \tag{1.1}$$

$$S_2[A_1, A_2] = \alpha_1 A_2 + \alpha_2 A_1^2, \tag{1.2}$$

$$S_3[A_1, A_2, A_3] = \beta_1 A_3 + \beta_2(A_2 A_1 + A_1 A_2) + \beta_3(\mathrm{tr}\, A_2)A_1, \tag{1.3}$$

$$S_4[A_1, A_2, A_3, A_4] = \gamma_1 A_4 + \gamma_2(A_3 A_1 + A_1 A_3) + \gamma_3 A_2^2 + \gamma_4(A_2 A_1^2 + A_1^2 A_2) + \gamma_5(\mathrm{tr}\, A_2)A_2 + \gamma_6(\mathrm{tr}\, A_2)A_1^2 + [\gamma_7\, \mathrm{tr}\, A_3 + \gamma_8(\mathrm{tr}\, A_1 A_2)]A_1 . \quad (1.4)$$

The stress tensors $S_{(N)}$ for fluids of grade N are determined when the coefficients which appear in the expressions for S_n are known. The objective of the experiments is to determine values for those coefficients (or combinations of coefficients) which appear in the analysis at the various orders.

2.1. Second-order results

When the free surface of the fluid makes a contact angle of 90° at the rod surface the height of climb of the fluid at the rod ($r = a$) is given at second order by the following approximate solution [2—4]:

$$h(a) = \frac{a\Omega^2}{2\,T\sqrt{S}}\left(\frac{4\,\hat{\beta}}{4+\lambda} - \frac{\rho a^2}{2+\lambda}\right) + O(\Omega^4), \quad (2)$$

where T is the surface tension, $S = \rho g/T$, $\lambda = a\sqrt{S}$, and $\hat{\beta} = 3\,\alpha_1 + 2\,\alpha_2$. Thus at small angular velocities Ω there is a linear relationship between $h(a)$ and Ω^2 from which the climbing constant $\hat{\beta}$ can be determined. We have performed extensive experiments with several samples of four different viscoelastic fluids (STP, TLA-227, Paratone 715, Polyacrylamide P-250 in glycerine and water), and we have always found a range of Ω for which the height rise is linear in Ω^2. However, our experiments were with a small number of fluids. It is quite likely that there are fluids that have no measurable second-order range. Recent experiments by Dealy and Vu [7] indicate that some molten polyethylene resins exhibit a linear region in Ω^2 at low rotation rates.

We have found that the 90° contact angle at the rod can be achieved using aluminum rods coated with Scotchgard. Accurate measurements of the height of climb can be obtained from photographic negatives taken at grazing incidence. Some typical results are shown in Fig. 1 for samples of TLA-227 and STP used in the concentric cylinder experiments described in Section 5 below. Two sets of measurements were made with STP, at temperatures which differed by approximately 5°C. For a fixed rod radius there is a distinct change in slope with temperature, and this is reflected in the value of $\hat{\beta}$. Figure 2 is a plot of $\hat{\beta}$ against temperature for a batch of STP used several years ago [4], and on this figure we have marked the values of $\hat{\beta}$ obtained from Fig. 1 for the STP we are using in our current experiments. Both fluids exhibit the same large decrease in the value of the climbing constant as the temperature is increased by just a few degrees.

A viscoelastic fluid will not always climb up a rotating rod. There is a critical radius [1,4] given by $r_c = 2\sqrt{\hat{\beta}/\rho}$, such that for $r < r_c$ normal stresses dominate, whereas for $r > r_c$ inertia forces dominate. Thus if the rod radius is greater than $2\sqrt{\hat{\beta}/\rho}$ the second-order theory predicts that the fluid will not

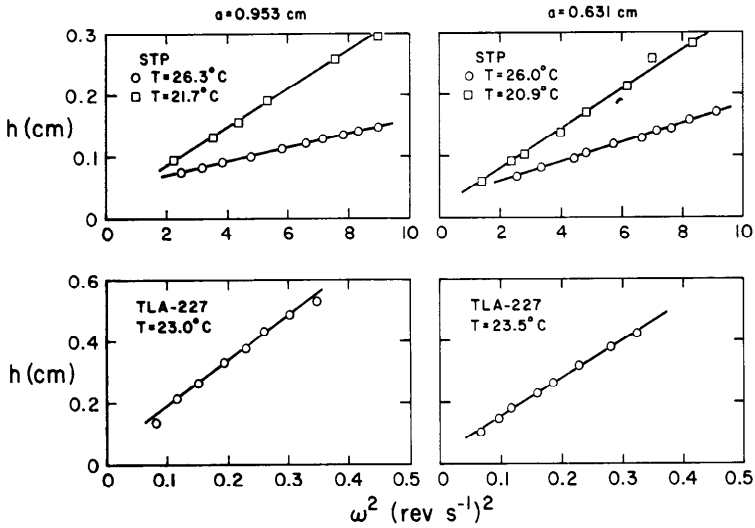

Fig. 1. The height of climb at the rod surface for a circular rod rotating in a large volume of viscoelastic fluid. The rotational speeds are limited to the second-order range (eqn. (2)).

climb up the rod. This is illustrated in Fig. 3, which shows the same rod (a = 0.476 cm) rotating at the same speed (5.0 rev/sec) in the same batch of STP at three different temperatures. At 56°C, $\hat{\beta}$ is approximately 0.03 and the

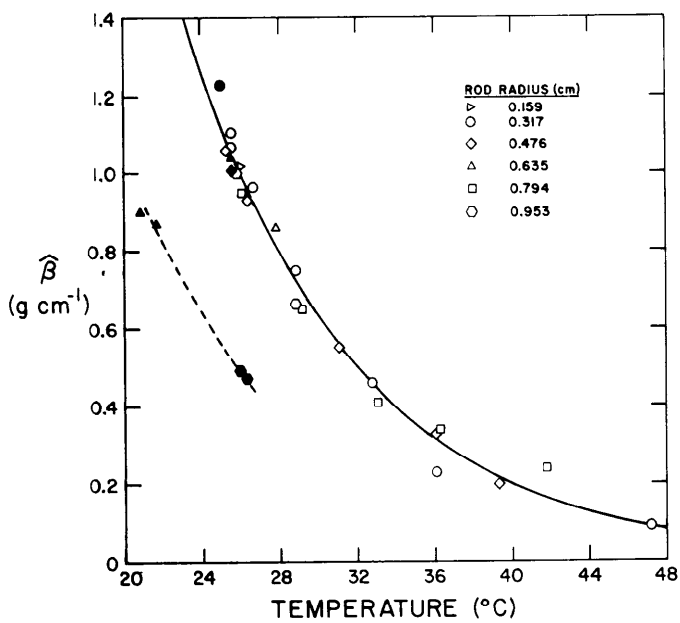

Fig. 2. The variation of the climbing constant $\hat{\beta}$ with temperature for two samples of STP.

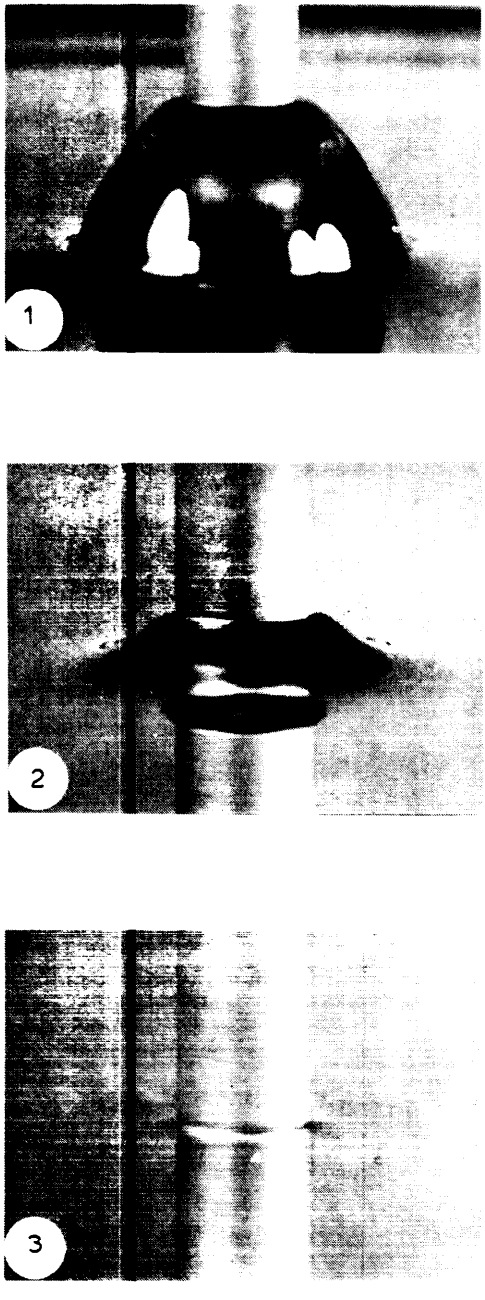

Fig. 3. The steady climb of STP on a rod of radius 0.476 cm rotating at 5.0 rev s^{-1} at three different temperatures: (1) 10°C; (2) 25°C; (3) 56°C. At 56°C the critical radius is less than the rod radius, and the fluid does not climb at any speed. (Pictures taken from [16]).

corresponding critical radius is approximately 0.37 cm, which is less than the rod radius.

2.2. Higher-order results

The higher-order theory of rod-climbing has been completed through fourth order [5,6] and is reviewed in [1]. The theory shows that at second order the free surface changes shape without generating secondary motions. The departure from flatness of the free surface at order two requires that the circumferential velocity, at order three, should depend on the depth. This vertical stratification of circumferential velocity induces torques in azimuthal planes at fourth order which lead to secondary motions.

In the second-order theory there is only one viscoelastic parameter, $\hat{\beta}$, whereas at fourth order the response of any viscoelastic fluid to steady rotation depends on the viscosity and on four viscoelastic parameters, namely $\hat{\beta} = 3\,\alpha_1 + 2\,\alpha_2$, $\hat{\alpha} = \alpha_1 + \alpha_2$, $\hat{\mu} = \beta_2 + \beta_3$, and $\hat{\gamma} = \gamma_3 + \gamma_4 + \gamma_5 + \frac{4}{7}\,\gamma_6$. These constants may be determined sequentially. We first find $\hat{\beta}$ from height rise measurements at the smallest values of the angular velocity Ω. The circumferential velocity at third order depends only upon $\hat{\beta}$ and $\hat{\mu}$, and thus $\hat{\mu}$ can be determined from measurements of the distribution of circumferential velocity at the smallest values of Ω. Finally the two remaining parameters $\hat{\alpha}$ and $\hat{\gamma}$ can be determined from measurements of free surface profiles at slightly larger values of the angular velocity. In this way all four viscoelastic parameters which characterize the Weissenberg effect through order four can be determined from experimental measurements utilizing the Weissenberg effect alone.

To investigate the feasibility of the above procedure we measured circumferential velocity profiles in three fluids using a technique similar to that employed by Hoffman and Gottenberg [8] for the measurements of circumferential velocities between concentric rotating cylinders. The fluid surface was illuminated with stroboscopic lighting at a known flashing rate. Small aluminum particles were dropped on the surface and multiple-image photographs were taken using a 500 mm telephoto lens. Circumferential velocity distributions for three different rods at several rotational speeds are reported in reference [6]. The results for STP are reproduced here in Fig. 4. The procedure for the determination of $\hat{\mu}$ was to use the theory to find a value which gave the best fit with experimental results for the two lowest rotational speeds of the 0.9525 cm rod. We fit the calculated curves to the experimental data at two rotational speeds because the calculated distributions are quite sensitive to changes in $\hat{\mu}$. Having found a value for $\hat{\mu}$ in this way we proceeded to use this value to compute the theoretical circumferential velocity distributions corresponding to all the remaining experimentally measured distributions. We found a value of $\hat{\mu} = -0.010$ g s cm^{-1} for this sample of STP, the negative sign indicating that the STP, which is a solution of polyisobutylene in oil, is slightly shear thinning. This is in agreement with the results of Hoffman and

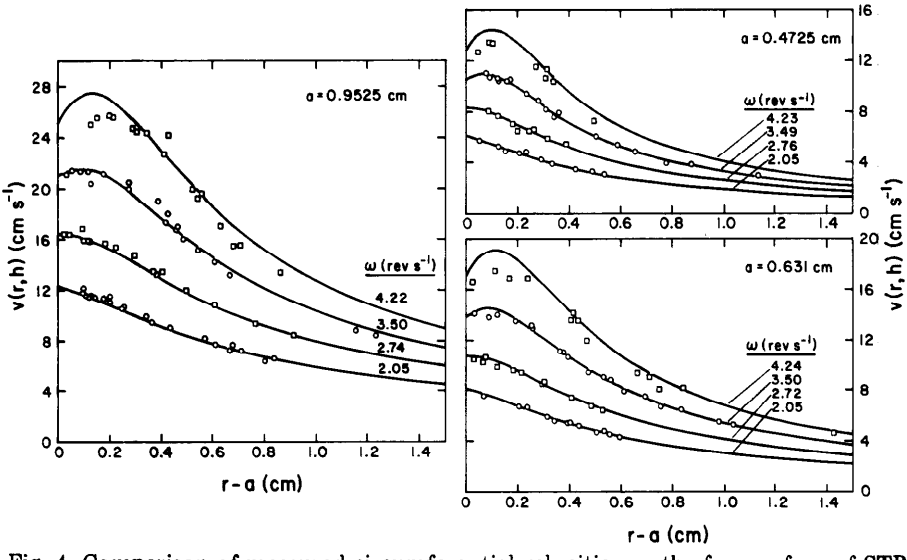

Fig. 4. Comparison of measured circumferential velocities on the free surface of STP with values predicted using third-order theory. The curves are identified by rod rotational speed ω. $\hat{\beta} = 0.89$ g cm^{-1}; $\hat{\mu} = -0.010$ g s cm^{-1}. The value of $\hat{\mu}$ was chosen by finding the best fit between theory and experiment for the two lowest rotational speeds of the 0.9525 cm rod.

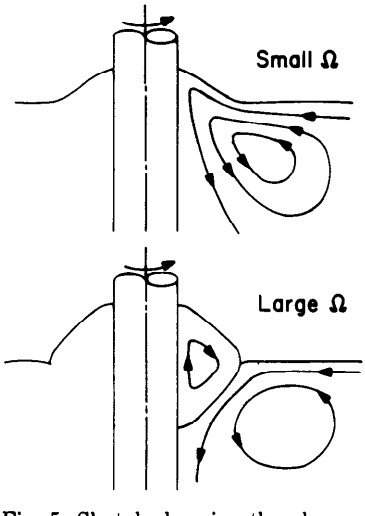

Fig. 5. Sketch showing the change in the secondary flow pattern from a single large eddy at small rod rotational speeds to a pattern consisting of a large eddy and a small eddy at higher rotational speeds. The secondary motion in the bubble changes direction, and at higher rotational speeds it is driven by the motion in the large eddy.

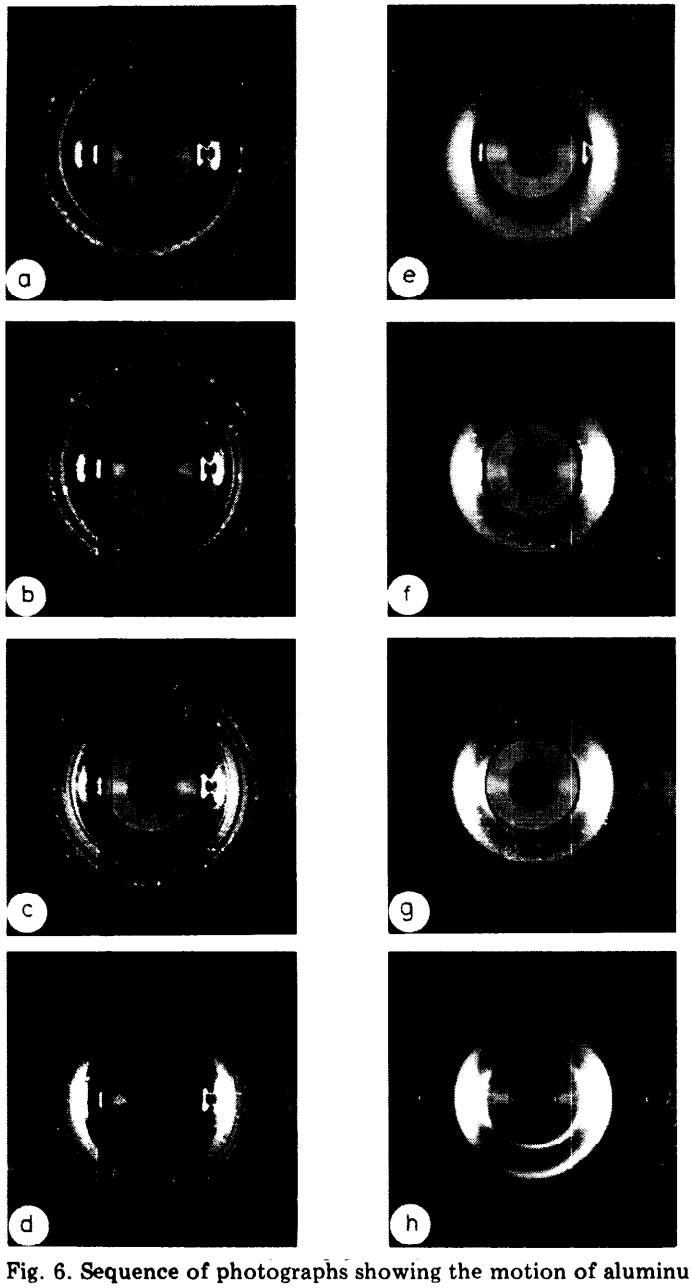

Fig. 6. Sequence of photographs showing the motion of aluminum flakes on the surface of TLA-227 for a rod of radius 0.9525 cm rotating at a speed $\omega = 0.49$ rev s^{-1}. The motion is viewed from above. The aluminum flakes start beyond the bubble radius and spiral radially inwards (i.e. up the surface of the bubble) towards the rod.

	(a)	(b)	(c)	(d)	(e)	(f)	(g)	(h)
Time (sec)	0	10	30	54	97	177	241	275 .

Gottenberg [8] for a solution of polyisobutylene in cetane. Their measured distributions are like ones which the perturbation theory would predict for a small negative value of $\hat{\mu}$.

The secondary motion induced by the rotation of the rod appears first at fourth order. Calculations show that at low rotational speeds the secondary motion appears as a circulation which moves the fluid near the free surface in towards the rod while the fluid further below the surface is forced away from the rod, as indicated in the top part of Fig. 5. In this configuration the

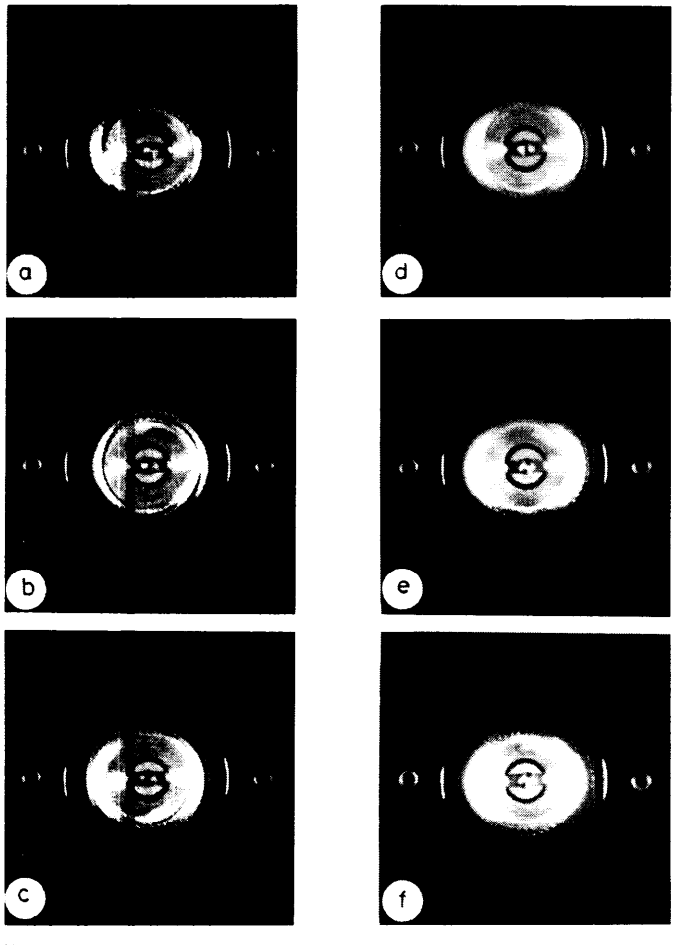

Fig. 7. Sequence of photographs showing the motion of aluminum flakes on the surface of TLA-227 when the rod in Fig. 6 rotates at $\omega = 1.12$ rev s^{-1}. The aluminum flakes start close to the rod and rapidly spiral down the bubble (radially outwards) to the outer edge of the bubble, where they disappear beneath the surface of the fluid.

	(a)	(b)	(c)	(d)	(e)	(f)
Time (sec)	0	4.5	10	17.5	24	44 .

bubble is held up by static forces associated with the circumferential shearing motion, and the secondary motions are driven in an anticlockwise sense by the "big torque" associated with the vertical stratification of inertia and normal stresses. At higher angular velocities the experiments of Saville and Thompson [9], and of Hoffman and Gottenberg [8], and our own experiments indicate the development of a "little torque" in the bubble, but not in the body of the fluid, which drives a "little clockwise eddy" on the top of the "big counterclockwise eddy" in the body of the fluid, as shown in the lower part of Fig. 5. The presence of two eddies probably correlates with the persistent indentation of the free surface which is nearly always observed in climbing experiments when Ω is large. The fluid now moves down the free surface of the bubble towards the outer edge.

The two types of secondary motion are demonstrated in Figs. 6 and 7. These show the motion, as viewed from above, of aluminum flakes on the surface of TLA-227. In Fig. 6 the rod rotational speed is 0.49 rev/sec. The aluminum flakes start well outside the bubble and slowly spiral inwards to the rod, moving up the free surface of the bubble. Figure 7 shows the same experimental configuration with the rotational speed increased to 1.12 rev/sec. Aluminum flakes, which were initially deposited on the bubble next to the rod, now spiral to the outer edge of the bubble where they disappear from view below the free surface of the fluid.

2.3. The breathing instability

There is a certain critical steady rotational speed of the rod at which the steady axisymmetric climb loses stability to a small-amplitude axisymmetric time-periodic motion in which the climbing bubble is alternately filled and emptied of fluid by a pumping mechanism associated with the secondary flow. This is illustrated in Fig. 8 which shows a sequence of pictures at 0.15 second intervals during one cycle of the time-periodic motion of a bubble of STP on a rod rotating at a constant angular speed of 19 rev/sec. It appears that the strong secondary motions which occur at high rotation rates carry the lower angular momentum fluid from the outside of the bubble towards the rod while the higher angular momentum fluid near the rod is pushed outwards by centripetal acceleration. A bulge of fluid grows (frames 1—4) which is supported from below by normal stresses and from the side by increasingly strong surface tension forces generated by the high curvatures of the bulge. Eventually the accumulated fluid in the bulge is sufficiently heavy to be dragged down by gravity (frames 5—9), and the fluid content of the bubble is decreased. The motion then begins again (frames 10—12). The filling and emptying of the bubble is somewhat analogous to the motion of the lung in breathing, which leads to the name "breathing instability". The instability appears to lead to a time-periodic bifurcating solution of Hopf's type in which the amplitude and frequency of the motion change continuously with changing rod rotational speed.

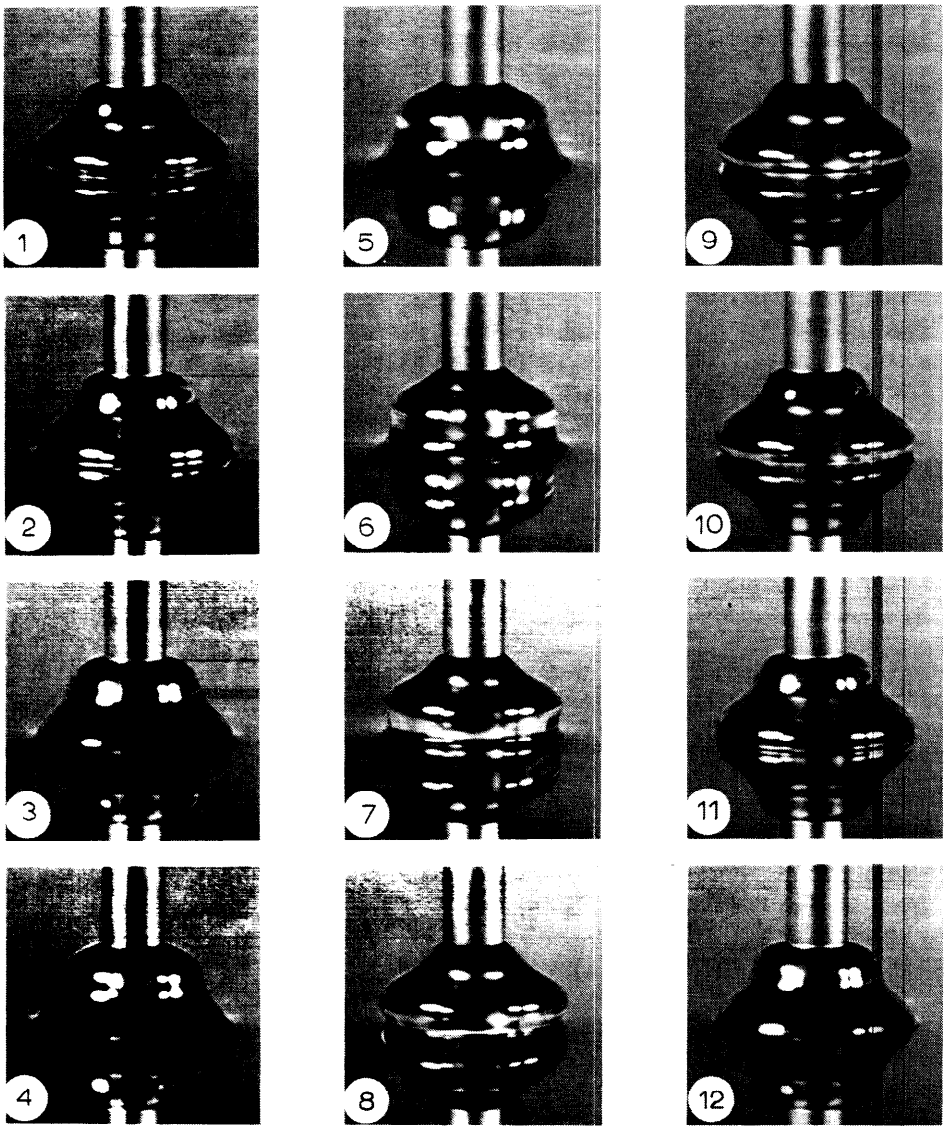

Fig. 8. The breathing instability of a bubble of STP on a rod of radius 0.476 cm rotating at 19 rev s^{-1}. Frames 1—10 represent one complete cycle. Time between frames = 0.15 sec. (Pictures taken from [16]).

3. Unsteady rod climbing

In this section we review recent extensions [11,12] of our original work [10] on the motion of a viscoelastic fluid induced by the torsional oscillations of a circular rod.

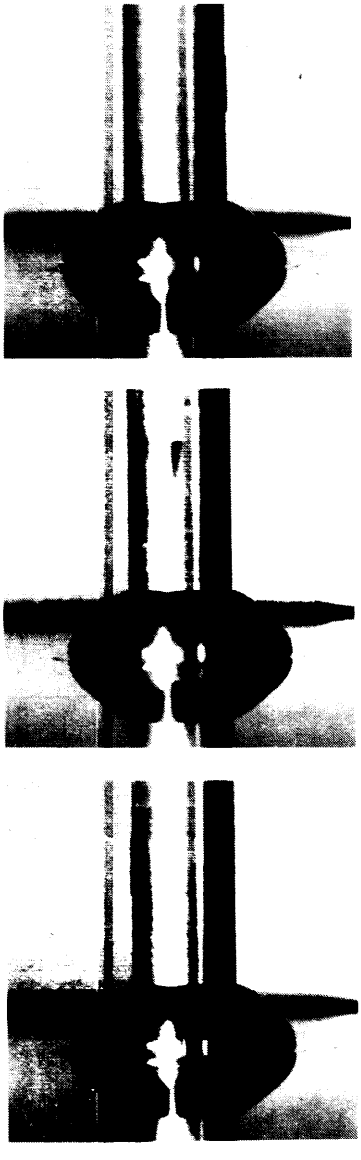

Fig. 9. The climb of TLA-227 on a rod of radius 0.636 cm oscillating at 4.2 cycles per second through an angle of twist of 2.91 radians. The black mark on the rod shows three different angular displacements of the rod during an excursion through a half cycle. The mean climb dominates the whole climb. The oscillatory part of the climb is not visible.

3.1. Stable configuration

A circular rod of radius a is made to oscillate with a motion $\Omega = \epsilon \sin \omega t$. The perturbation analysis of this problem is a small amplitude theory, with

amplitude $\epsilon = \omega\Theta/2$, where Θ is the angle of twist. The analysis has been summarized in [1], and only the essential results will be quoted here.

At second order, the height of climb at the rod, $h(a, t, \epsilon)$, is given by:

$$h(a, t, \epsilon) = \tfrac{1}{4}\,[2\,\bar{\bar{h}}(a) + e^{2i\omega t}\,h_1(a) + e^{-2i\omega t}\,\bar{h}_1(a)]\epsilon^2 + O(\epsilon^4),$$

where $(\bar{\bar{\ }})$ denotes average values over an oscillation period $2\,\pi/\omega$, and $(\bar{\ })$ denotes the complex conjugate. The climb $h(a, t, \epsilon)$ consists of the superposition of a mean climb, $\bar{\bar{h}}(a)$ independent of t, and an oscillating climb which oscillates with a frequency of $2\,\omega$. All our experiments so far [10—12] show that the mean climb completely dominates the total climb at each and every instant except for very high values of both the oscillation frequency and angle of twist. Figure 9 shows three different angular displacements of a rod during an excursion through a half cycle during a small amplitude motion. The oscillatory part of the climb is not visible. The mean, steady, climb is given approximately at second order by

$$\bar{\bar{h}}(a) = \frac{\omega^2\Theta^2}{8}\left(\frac{a}{\sqrt{\rho g T}}\,\frac{|\Lambda + 1|^2\hat{\beta}_\Lambda}{(\Lambda_r + 1)[2(\Lambda_r + 1) + \lambda]} - \frac{\rho a^2}{2\,\Lambda_r(2\,\Lambda_r + \lambda)}\right), \tag{3}$$

where $\lambda^2 = \rho g a^2/T$ and

$$\hat{\beta}_\Lambda = -(2\,\Lambda_r + 1)\int_0^\infty G(s)\,\frac{\sin\omega s}{\omega}\,ds$$

$$+ (\Lambda_r + 1)\int_0^\infty\int_0^\infty \gamma(s_1, s_2)\cos\omega(s_1 - s_2)\,ds_1\,ds_2, \tag{4}$$

and Λ_r is the real part of a complex function Λ of the material function $G(s)$. Equation (3) shows that, for small amplitude motions (i.e., small ϵ), the normalized mean climb at the rod, given by

$$H(a, \omega) = \bar{\bar{h}}(a, \epsilon)/\Theta^2,$$

is independent of the angle of twist Θ, and is a universal function of the frequency ω.

To obtain approximations to the material functions $G(s)$ and $\gamma(s_1, s_2)$ from measurements of the rise curve $H(a, \omega)$ we approximate the functions with generalized Maxwell models:

$$G(s) \approx \frac{-\mu^2}{\alpha_1}\sum_1^N \frac{a_n^2}{b_n}\exp\left(\frac{\mu}{\alpha_1}\frac{a_n}{b_n}\,s\right), \tag{5}$$

$$\gamma(s_1, s_2) \approx \alpha_2\sum_1^M c_n k_n^2\exp(-k_n(s_1 + s_2)), \tag{6}$$

where

$$\sum_{1}^{N} a_n = \sum_{1}^{N} b_n = \sum_{1}^{M} c_n = 1 . \tag{7}$$

There are $2N + 2M - 3$ unknown constants to be determined if the constants μ, α_1 and α_2 of the fluid of second grade are known. The unknown constants associated with the first three approximations are

$N = 1, M = 1$ $\quad k_1$;

$N = 1, M = 2$ $\quad k_1, k_2, c_1$;

$N = 1, M = 3$ $\quad k_1, k_2, k_3, c_1, c_2$.

Our original experiments [10] were performed with a single rod in a sample of TLA-227. The results are reproduced in the upper part of Fig. 10, where it can be seen that the experimental points define part of the universal curve until they break away at some value of the oscillation frequency ω. We conclude that the points which break away from the universal curve are manifestations of effects which are induced by terms of order higher than second. Then, by choosing $k_1^2 = 15.43$ we were able to fit the $(N = 1, M = 1)$ model for ω^2 values up to 30 (rad/sec)^2, and by choosing $k_1^2 = 14.50$, $k_2^2 = 307.0$ and $c_1 = 0.9735$ we were able to fit the $(N = 1, M = 2)$ model for ω^2 values up to 450 (rad/sec)^2.

In our latest experiments [11,12] we have tested the analysis on another sample of TLA-227 and on a sample of Paratone 715 using several different rods. In addition, we have attempted to fit the experiments to higher order models in the (N, M) sequence. In Fig. 11 we summarize our latest results with TLA-227; the Paratone 715 results are very similar. The figure shows results for three rod radii, where for clarity only the experimental points which lie on the universal curve have been included. The decision concerning which points to include was based upon a conservative estimate for the region of validity of the second-order theory, which we established in reference [10]. We then attempted to fit the (1,1), (1,2) and (1,3) models to the universal experimental curves, and arrived at the following values for the unknown coefficients:

(N,M)	(1,1)	(1,2)	(1,3)
	$k_1^2 = 16$	$k_1^2 = 15.2$	$k_1^2 = 15.2$
		$k_2^2 = 310.0$	$k_2^2 = 310.0$
		$c_1 = 0.976$	$k_3^2 = 2000$
			$c_1 = 0.978$
			$c_2 = 0.0184$.

The theoretical predictions for the three rods have been brought together in

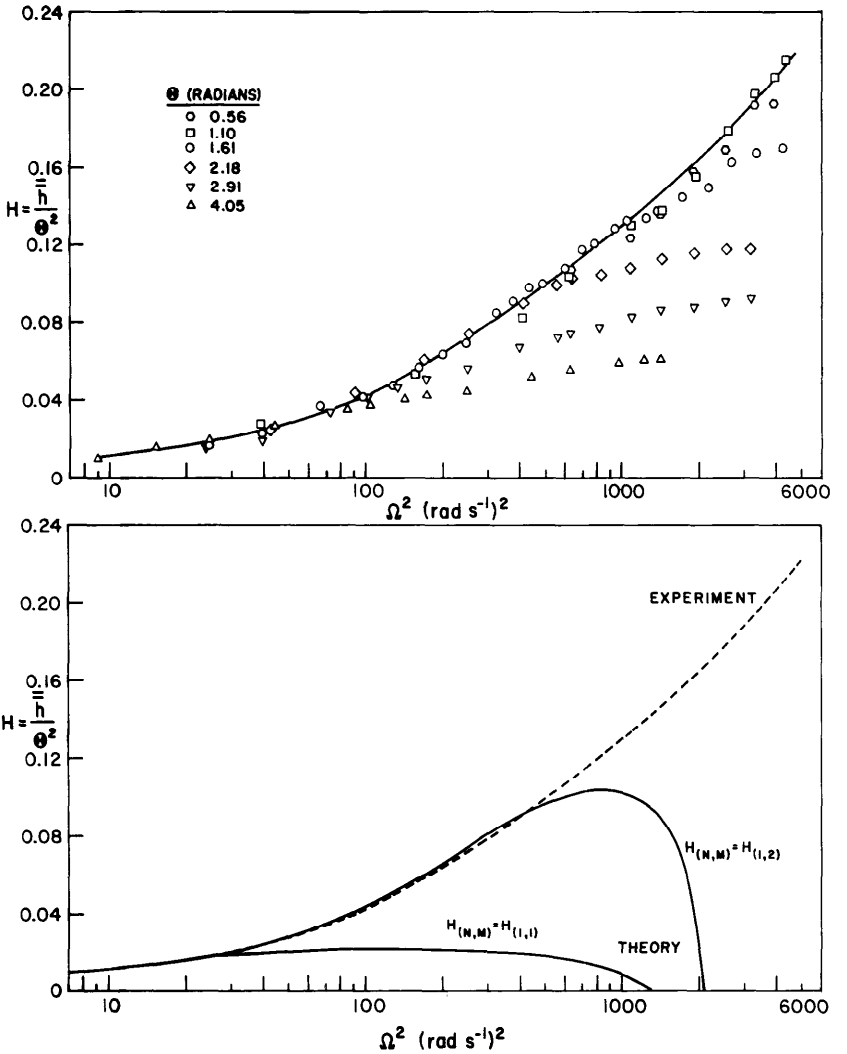

Fig. 10. The normalized height rise as a function of the frequency of oscillation for a rod of radius 0.636 cm in TLA-227. Experimental points belonging to six different angles of twist are shown. The experimental normalized rise at second order obtained from the upper part is compared with the predictions of the generalized Maxwell model in the lower part, [10].

the fourth part of Fig. 11 to show the rather weak dependence on rod radius.

We do not claim or believe that the Maxwell models we have chosen are the best representations of the material functions. Although it is possible to find values for the unknown coefficients which will fit the theory to the experimentally measured universal curve, the choosing of the coefficients becomes very laborious at the higher (N,M) models. We should also point out that, for

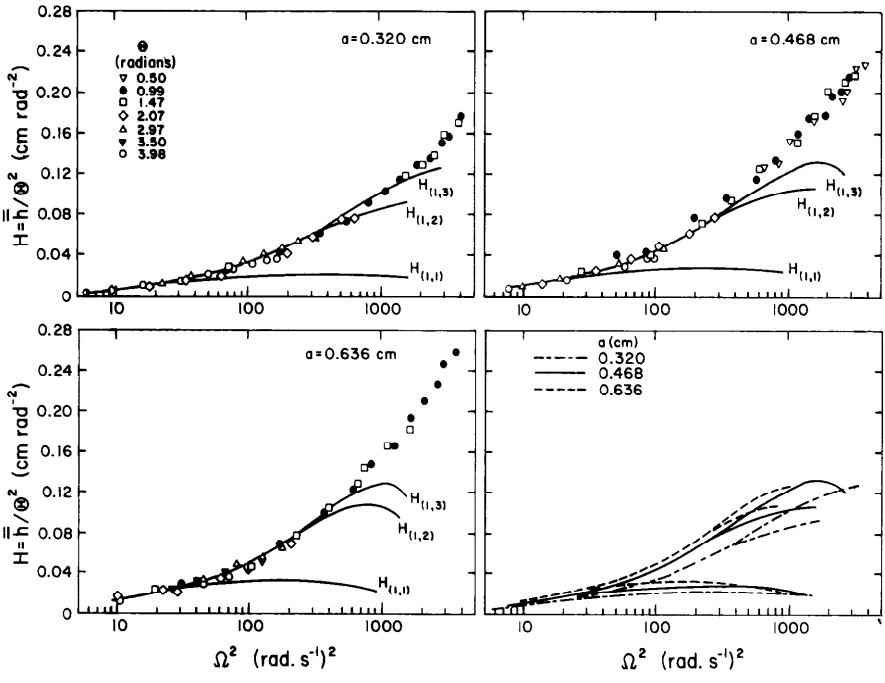

Fig. 11. The normalized height rise as a function of the frequency of oscillation for three rods in TLA-227. Only experimental points which define the universal curves are shown. Predictions from the first three members of the sequence of generalized Maxwell models are included.

the fluids we have used, we have not been able to find any values for a_n and b_n in eqn. (5) which improve the fit over that obtained using $a_n = 1$, $b_n = 1$. In other words, the best fits we have been able to find have been for the case $N = 1$ in eqn. (5).

Temperature effects caused by shear heating of the fluid were of prime concern to us throughout these experiments. We continuously monitored the fluid temperature at the surface of the rods by means of thermocouples which were mounted flush with the rod surface. Some typical plots of temperature rise against elapsed running time are shown in Fig. 12 for a single rod which was oscillated at fixed frequencies in TLA-227. It is clear that there is a rapid increase in temperature of the fluid near the rod during the first few minutes of operation. Based on these findings we developed an experimental procedure by which we could collect data rapidly and at the same time keep the net temperature change of the fluid at the rod surface to less than 1°F through the course of a complete experimental run.

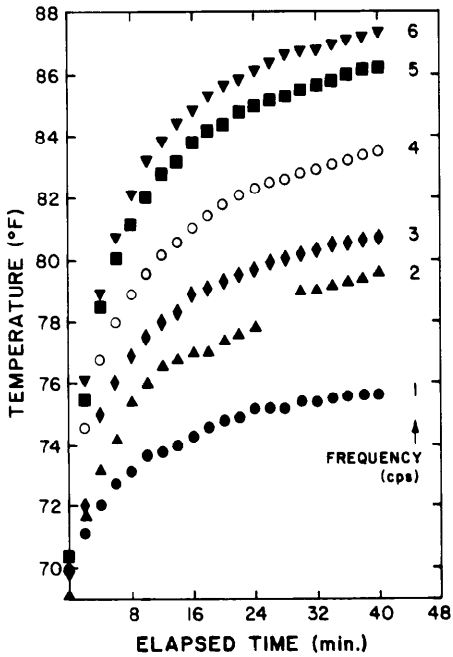

Fig. 12. Temperature of the fluid at the rod surface as a function of time when a rod of radius 0.468 cm is oscillated through an angle of twist of 3.98 radians in TLA-227.

3.2. The flower instability

When the amplitude ϵ is small the motion is axisymmetric and periodic with period $2\pi/\omega$. There is a mean climb and a superposed oscillation of frequency 2ω. For larger values of ω the axisymmetric solution loses stability to another solution with a different symmetry pattern. The new symmetry pattern has a certain integral number of lobes, formed like the petals of a flower. The frequency of oscillation of the petals of the flower is ω. There is a phase lag which is determined at each radius by an outgoing wave which is supported by fluid elasticity. Mathematically we can characterize the flower instability as a symmetry breaking T-periodic bifurcation of a T-periodic flow.

The growth of the instability for a rod oscillating at 7 cycles per second in TLA-227 is illustrated in Fig. 13. The photographs show the rod at approximately the same position in its cycle, and the time between successive photographs is approximately 1.1 seconds. Figure 14 shows the motion of the fully-developed three-lobe pattern as the rod goes through one complete cycle of its motion. We have not investigated the mechanics of the instability and the parameters which lead to the number of lobes which are formed. For example, with TLA-227 we have been able to produce both three- and four-lobe patterns from what appear to be identical operating conditions [13], whereas

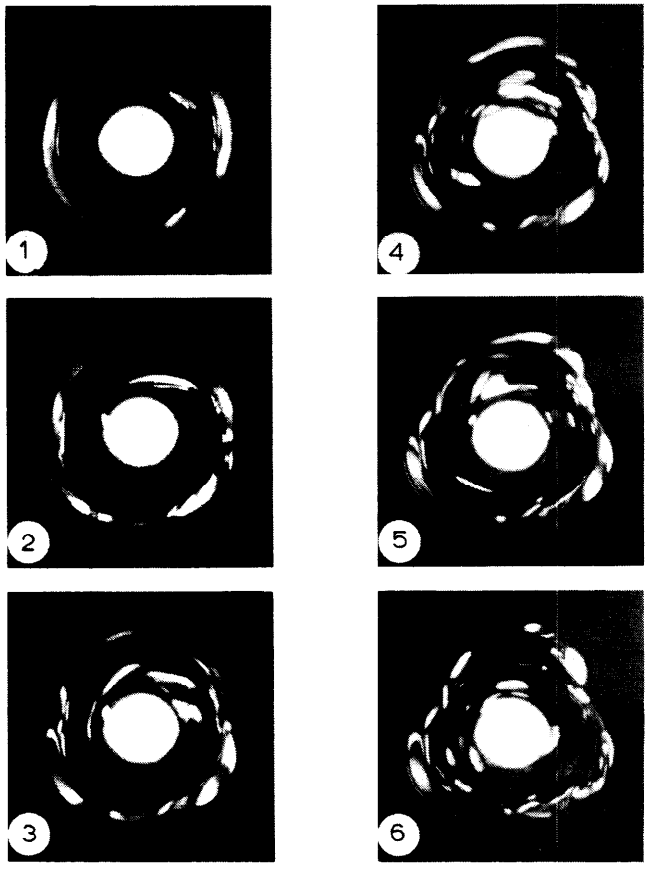

Fig. 13. The growth of the flower instability in TLA-227 as viewed from above. The angle of twist is 4 radians and the frequency of oscillation is 7 cycles per sec. The photographs show the rod at approximately the same position in its cycle. The time between photographs is approximately 1.1 sec. (Pictures taken from [16]).

with Paratone 715 (which has approximately the same surface tension and climbing constant as TLA-227, but a somewhat higher shear viscosity) a large number of petals always appears.

4. Normal stress amplification

We showed in [13] that normal stress effects may be amplified considerably by floating a viscoelastic fluid on water. The perturbation analysis of rod climbing for this layered configuration gives the following expressions for the height rises at the rod at second order:

$$h_{\text{top}} = \frac{a\Omega^2}{2\,T_T\sqrt{S_T}}\left(\frac{4\,\hat{\beta}}{4+\lambda_T} - \frac{(\rho-\rho_a)a^2}{2+\lambda_T}\right) + O(\Omega^4), \tag{8}$$

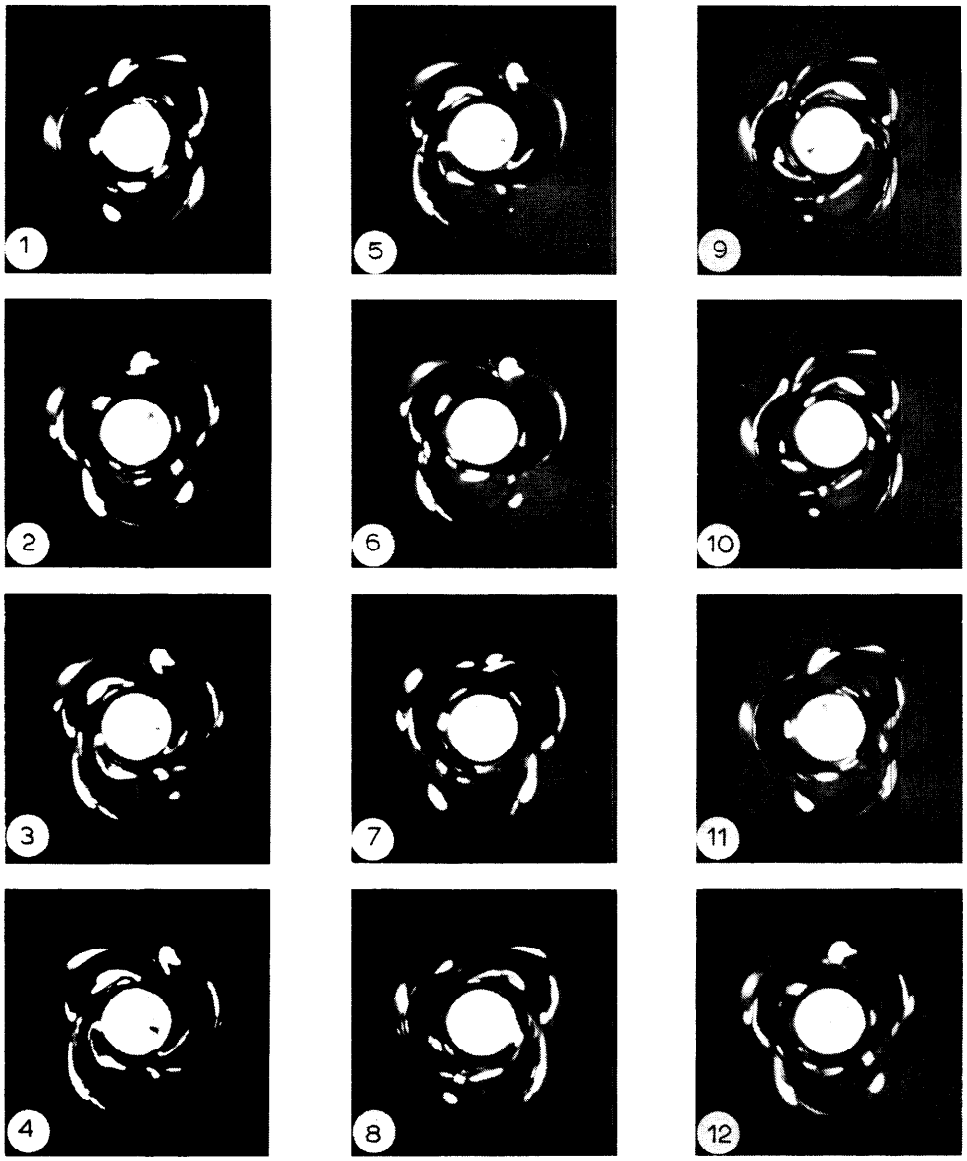

Fig. 14. The motion of the fully-developed three-lobe flower instability of Fig. 13 as the rod goes through one complete cycle. The time between frames is approximately 0.015 sec. (Pictures taken from [16]).

$$h_{\text{bottom}} = \frac{-a\Omega^2}{2\,T_B\sqrt{S_B}}\left(\frac{4\,\hat{\beta}}{4+\lambda_B} + \frac{(\rho_w-\rho)a^2}{2+\lambda_B}\right) + O(\Omega^4)\,, \tag{9}$$

where $\lambda = \omega\sqrt{S}$, $S_T = (\rho - \rho_a)g/T_T$, $S_B = (\rho_w - \rho)g/T_B$ and T_T is the surface

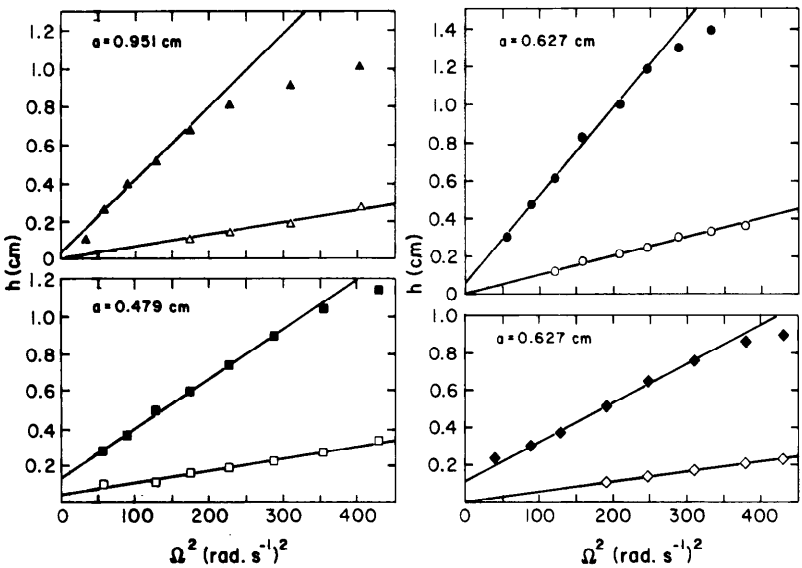

Fig. 15. Measured values of the height rise at the rod surface for a circular rod rotating in STP which floats on a layer of water. Open symbols correspond to the up-climb at the air interface, and filled symbols correspond to the down-climb at the water interface.

tension at the viscoelastic fluid/air interface and T_B is the interfacial tension at the viscoelastic fluid/water interface. Equation (8) shows that normal stresses elevate and inertia depresses the viscoelastic fluid at the air interface. At this interface there is a critical radius. Equation (9) shows that normal stresses and inertia have the same sign and both depress the viscoelastic fluid at the water interface. At this interface a critical radius does not exist. Experimental results for STP floating on water [13] are shown in Fig. 15. The values of $\hat{\beta}$ computed using equations (8) and (9) are listed below in Table 1. There is presumably only one value of $\hat{\beta}$ for this sample of STP at a given temperature. The values of $\hat{\beta}$ computed from the up-climb and from the down-climb for the different rods are in good agreement at a temperature of approximately 28°C.

TABLE 1

Rod radius (cm)	Temperature (°C)	$\hat{\beta}$ (g cm^{-1})	
		Air/STP	Water/STP
0.479	27.8	0.78	0.78
0.627	28.2	0.65	0.49
0.951	27.8	0.83	0.66
0.627	23.5	1.07	1.10

Equations (8) and (9) show that at low angular speeds the down-climb is larger than the up-climb, roughly in the ratio

$$\frac{h_B}{h_T} \approx \frac{\sqrt{T_T(\rho - \rho_a)}}{\sqrt{T_B(\rho_w - \rho)}} \left(\frac{4 + a\sqrt{(\rho - \rho_a)g/T_T}}{4 + a\sqrt{(\rho_w - \rho)g/T_B}} \right) . \tag{10}$$

For example, for STP floating on water the down-climb is about four times larger than the up-climb at low angular speeds. We can in principle achieve very large amplifications of the down-climb of the viscoelastic fluid by replacing the water by another Newtonian fluid having a density which is closer to that of the viscoelastic fluid.

When the rotational speed is increased beyond the second-order range the down-climbing bubble rapidly loses its equilibrium shape because of the large volume of fluid which is forced into the bubble by the amplified normal

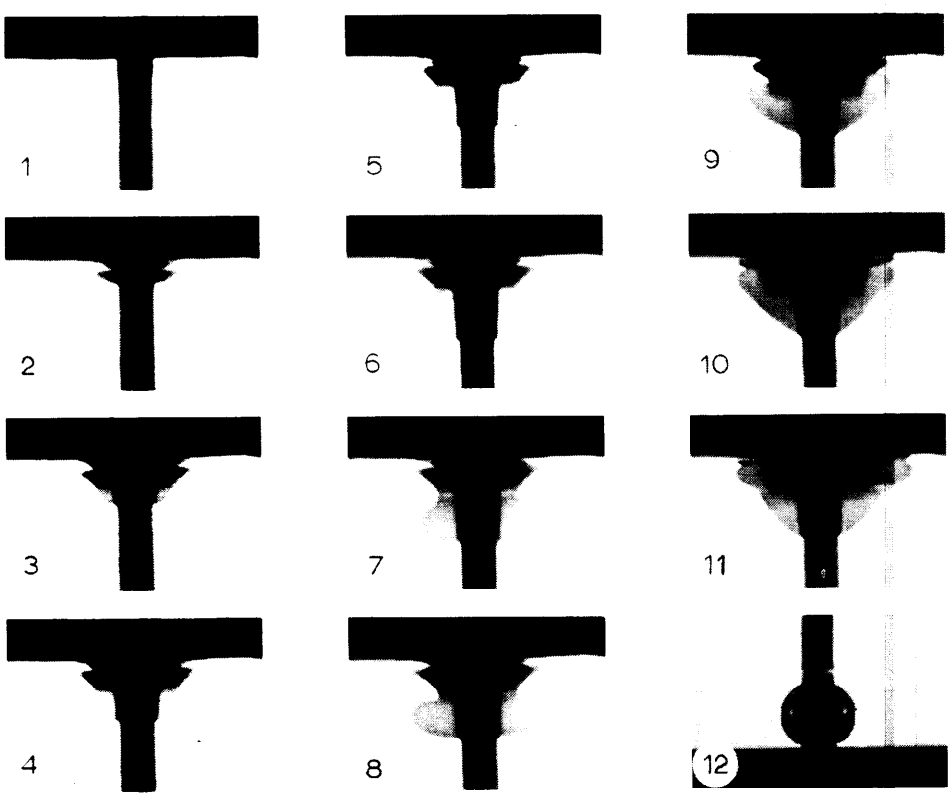

Fig. 16. The motion of the bubble of TLA-227 on a rod which rotates at 14.5 rev s^{-1} in TLA-227 floating on water. The periodic motion of the bubble is controlled by the competing effects of normal stresses, inertia, surface tension and buoyancy forces. The bubble on the upper surface of the TLA-227 (frame 12) is steady and stable. The time between frames is 6 sec. (Pictures taken from [16]).

stresses. This is illustrated in Fig. 16 which shows the down-climb of TLA-227 floating on water. The rod rotational speed is increased very rapidly to 1.45 rev/sec and then held constant. The bubble of TLA-227 at the air interface rapidly grows to the shape shown in frame 12, and remains steady with this shape. The TLA-227 at the water interface grows downwards under the action of normal stresses and inertia forces (frames 1—5). The bubble of viscoelastic fluid tries to form a toroidal figure of equilibrium in a balance between normal stresses, inertia, surface tension and buoyancy forces (frames 6—8). As more fluid is driven into the bubble, buoyance forces become dominant and cause the toroidal part of the bubble to float slowly upwards (frames 9—11). Normal stresses and inertia continue to force fluid into the now reduced bubble, and the cycle is repeated. This cyclic process may be another manifestation of the breathing instability, with "slow" breathing and with the motion upside-down compared with that at an air interface (Fig. 8).

The perturbation analysis for one viscoelastic fluid floating on a second viscoelastic fluid is a straightforward extension of that for the viscoelastic fluid floating on a Newtonian fluid. Equation (9) for the down-climb is replaced by

$$h_{\text{bottom}} \approx \frac{-a\Omega^2}{2\,T_B\sqrt{S_B}}\left(\frac{4(\hat{\beta}_U - \hat{\beta}_L)}{4 + \lambda_B} + \frac{(\rho_L - \rho_U)a^2}{2 + \lambda_B}\right) + O(\Omega^4), \tag{11}$$

where $S_B = (\rho_L - \rho_U)g/T_B$, "U" denotes the lighter fluid and "L" denotes the heavier fluid. The size of the climbing bubble is now determined by the relative magnitudes of the densities and the climbing constants. If the climbing constant of the lighter fluid is greater than that of the heavier fluid, a bubble of the lighter fluid will move down into the heavier fluid, with the size depending upon the density difference. If, on the other hand, the climbing constant of the heavier fluid is greater than that of the lighter fluid the inertia forces and normal stresses are again in opposition and the heavier fluid will climb into the lighter fluid. This situation is illustrated in Fig. 17 which shows a rod of radius 0.620 cm rotating at 3.2 rev/sec in a layer of STP floating on a layer of TLA-227. The density difference at the STP/TLA interface is very small:

$$\rho_{TLA} - \rho_{STP} = 0.896 - 0.891 = 0.005 \text{ g cm}^{-3},$$

and the difference in climbing constants is large:

$$\hat{\beta}_{TLA} - \hat{\beta}_{STP} \approx 20 - 1 \approx 19 \text{ g cm}^{-1}.$$

The gravity forces acting on the climbing bubble of TLA-227 are very small so that the large normal stresses are essentially unopposed. The TLA-227 climbs without bound, until it eventually climbs through the upper surface of the STP, where its motion is then limited by gravity. The surface of the climbing column of TLA-227 exhibits an interesting wrinkling effect whose origin may lie in a buckling instability.

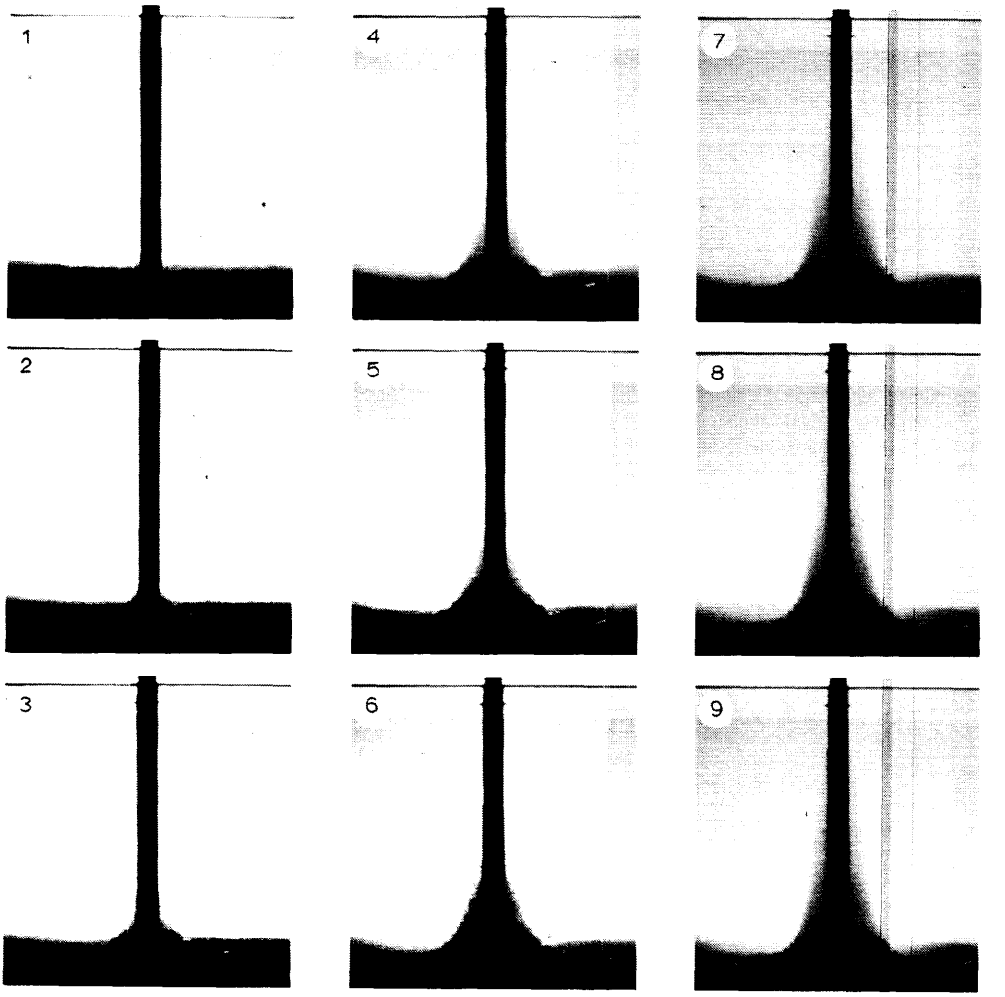

Fig. 17. The climb of TLA-227 on a rod of radius 0.620 cm for a configuration in which STP floats on TLA-227. The steady rotational speed is 3.2 rev s^{-1}. The density difference at the STP/TLA-227 interface is 0.005 g cm^{-3} and the difference in climbing constants is approximately 19 g cm^{-1}. The TLA-227 climbs without bound through the STP because the normal stresses have essentially no gravity forces to oppose them. Time between frames is approximately 7.5 sec. (Pictures taken from [16]).

5. Motion between concentric rotating cylinders

The free surface on a viscoelastic fluid contained between concentric rotating cylinders can exhibit a variety of shapes which depend upon the viscoelastic parameters characterizing the fluid, the radii of the two cylinders, and the speed of rotation. We have recently completed an experimental inves-

tigation of this problem [14] in which we used a stationary outer cylinder of fixed radius and four inner cylinders, each of different radius. Three viscoelastic fluids were employed, namely TLA-227, STP, and polyacrylamide in glycerine—water. Comparisons of the measured profiles with profiles predicted from the second-order theory showed excellent agreement at low angular velocities.

5.1. Second-order theory

The complete perturbation theory for this problem has been carried out through fourth order, and is reported in detail in [5] and [6]. To test the theory we compared experimental profiles with theoretical predictions at second order. Thus we review briefly here only those parts of the second-order theory which lead to predictions for the free surface profile.

The surface height $h(r; \Omega)$ is written in a power series in Ω in the usual way [1,2,4]:

$$h(r; \Omega) = \tfrac{1}{2}\,\Omega^2\, h^{[2]}(r_0) + O(\Omega^4), \tag{12}$$

where (r_0, z_0) are coordinates of the rest state defined in

$$\mathcal{V}_0 = \{r_0, \theta_0, z_0 | a \leqslant r_0 \leqslant b,\ 0 \leqslant \theta \leqslant 2\pi,\ -\infty < z_0 \leqslant 0\}\ .$$

The substantial derivative $h^{[2]}(r_0)$ is taken with respect to Ω at $\Omega = 0$ when r_0 and z_0 are fixed. Following the procedure described in [1] the equation for $h^{[2]}$ is

$$\frac{T}{r_0}\frac{\mathrm{d}}{\mathrm{d}r_0}\left(r_0\,\frac{\mathrm{d}h^{[2]}}{\mathrm{d}r_0}\right) - \rho g h^{[2]} + \Phi^{(2)} = 0 \qquad \text{at} \qquad z = 0, \tag{13}$$

where $h^{[2]}$ satisfies one of the pairs of boundary conditions

$$\frac{\mathrm{d}h^{[2]}(a; \Omega)}{\mathrm{d}r} = \frac{\mathrm{d}h^{[2]}(b; \Omega)}{\mathrm{d}r} = 0, \tag{14.1}$$

$$h^{[2]}(a; \Omega) = h^{[2]}(b; \Omega) = 0, \tag{14.2}$$

$$\frac{\mathrm{d}h^{[2]}(a; \Omega)}{\mathrm{d}r} = h^{[2]}(b; \Omega) = 0, \tag{14.3}$$

$$h^{[2]}(a; \Omega) = \frac{\mathrm{d}h^{[2]}(b; \Omega)}{\mathrm{d}r} = 0\ . \tag{14.4}$$

The derivative $\Phi^{(2)}$ appearing in eqn. (13) is the derivative of the total head Φ taken with respect to Ω at $\Omega = 0$ when r and z are fixed.

It is convenient for computational purposes to work in terms of dimensionless quantities. To do this we introduce the following dimensionless quantities:

$$t = 2\,r_0/(b - a), \qquad \eta = a/b,$$

$$\hat{S} = \rho g b^2(1 - \eta^2)/4T\ , \qquad \hat{R} = 4\hat{\beta}/\rho b^2 \eta^2\ .$$

The derivatives $h^{[2]}$ and $\Phi^{(2)}$ may then be written in the form

$$\frac{gh^{[2]}(r_0)}{b^2\eta^2} = H_{21}(t) + \hat{R}H_{22}(t), \tag{15}$$

$$\frac{\Phi^{(2)}(r_0)}{\rho b^2\eta^2} = \Phi_{21}(t) + \hat{R}\Phi_{22}(t)\,. \tag{16}$$

In writing equations (15) and (16) we have used the principle of superposition to reduce the solution to the computation of functions of η and $\hat{S}$ alone. For fixed values of the group $\rho g/T$, the prescription of η and $\hat{S}$ is equivalent to prescribing the radii of the inner and outer cylinders. Hence when $\rho g/T$ is fixed the dimensionless functions are independent of material parameters.

The height rise functions in eqn. (15) satisfy

$$\frac{1}{t}\frac{\mathrm{d}}{\mathrm{d}t}\left(t\frac{\mathrm{d}H_{2i}}{\mathrm{d}t}\right) - \hat{S}H_{2i} + \hat{S}\Phi_{2i}(t) = 0, \qquad i = 1, 2 \tag{17}$$

and one pair of the four possible boundary conditions (14.1)—(14.4). The functions $\Phi_{21}(t, \eta)$ and $\Phi_{22}(t, \eta)$ can be found explicitly:

$$\Phi_{21}(t, \eta) = \frac{\eta^2}{(1-\eta^2)^2}\left((1-\eta)^2t^2 - 4\ln\frac{(1-\eta)t}{2\eta} - \frac{4}{(1-\eta)^2t^2}\right) - \frac{6\eta^2\ln\eta}{(1-\eta^2)^3}$$
$$- \frac{2\eta^2(2+\eta^2)}{(1-\eta^2)^2} - \frac{1}{2\hat{S}(1+\eta)^2}\left(t\frac{\mathrm{d}H_{21}}{\mathrm{d}t}\right)\Bigg|_a^b,$$

$$\Phi_{22}(t, \eta) = \frac{16\eta^4}{(1-\eta^2)^2(1-\eta^4)t^4} - \frac{\eta^2}{(1-\eta^2)^2} - \frac{1}{2\hat{S}(1+\eta)^2}\left(t\frac{\mathrm{d}H_{22}}{\mathrm{d}t}\right)\Bigg|_a^b.$$

Thus, when $\hat{S}$ and η are given, eqns. (17) can be solved numerically using the appropriate boundary conditions to yield the shape of the free surface of the fluid.

5.2. Experimental results

We summarize here our results with TLA-227 and STP, which exhibit very different free surface shapes for our experimental apparatus. The free surface on polyacrylamide in glycerine—water shows a similar behavior to STP.

The stationary outer cylinder of our apparatus had a radius of 8.588 cm. Four different inner cylinders were used, having radii of 3.936, 5.018, 5.704, and 6.477 cm. The cylinders were very carefully machined to insure roundness, and the equipment was assembled with the aid of a specially designed gage which could measure the clearance between the cylinders to within 0.0001 cm. Surface profiles were measured using a micrometer-mounted needle, which was traversed across the gap, and observed through a travelling microscope. A complete description of the equipment is given in [14].

Theoretically-predicted free surface profiles for the TLA-227 sample used to construct Fig. 1 are shown in Fig. 18 for the four inner cylinders which were employed in our experiments and for four smaller inner cylinders. The profiles are those corresponding to a rotational speed of 0.16 rev/sec. Two

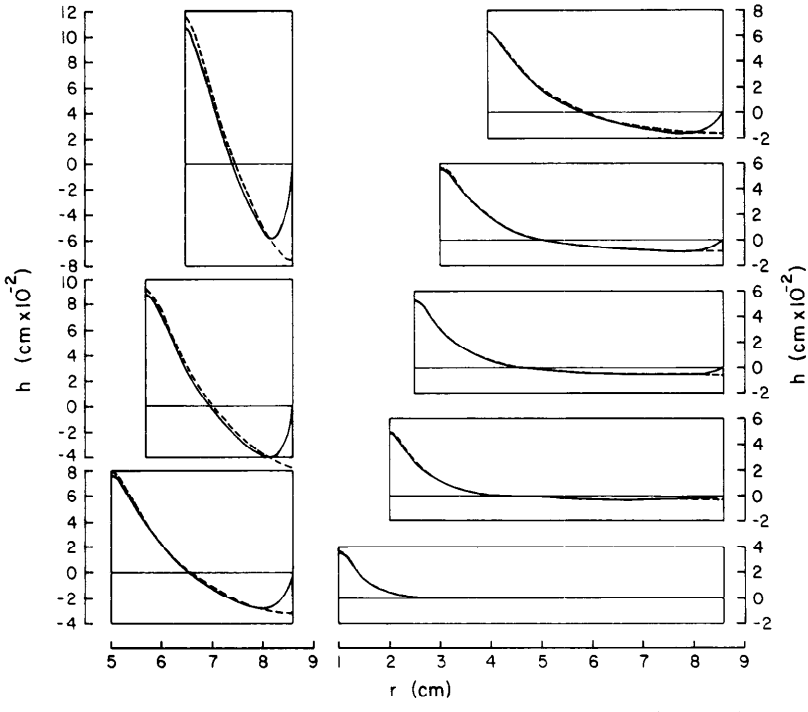

Fig. 18. The free surface on TLA-227 between concentric cylinders for a stationary outer cylinder of radius 8.588 cm and various inner cylinders rotating at 0.16 rev s^{-1}. — — —, zero slope boundary condition at both walls; ———, fixed point of attachment at the outer cylinder.

profiles are shown for each inner cylinder, one associated with the zero slope boundary condition at both the inner and outer walls, and the second associated with the zero slope boundary condition at the inner cylinder and a fixed point of attachment at the outer cylinder. The climbing constant for TLA-227 is large (29.0 gram cm^{-1}), and the predicted profiles are those which we would anticipate from the Weissenberg effect, with the fluid climbing up the inner cylinder and being depressed near the outer cylinder. It is clear from Fig. 18 that the boundary condition at the outer cylinder has little effect on the shape of the climbing fluid except for small clearances between the two cylinders.

Comparisons of experimentally-measured profiles with predicted profiles are presented in Fig. 19 for the four inner cylinders operating at five different rotational speeds. We have observed in all our experiments with the four viscoelastic fluids we have used that once a surface has been wetted with the fluid there always remains a thin coating of the fluid on the surface. For this reason the appropriate boundary condition at the outer cylinder is the fixed contact line condition. It appears from Fig. 19, however, that the analysis predicts a somewhat thicker layer of fluid on the outer cylinder than observed

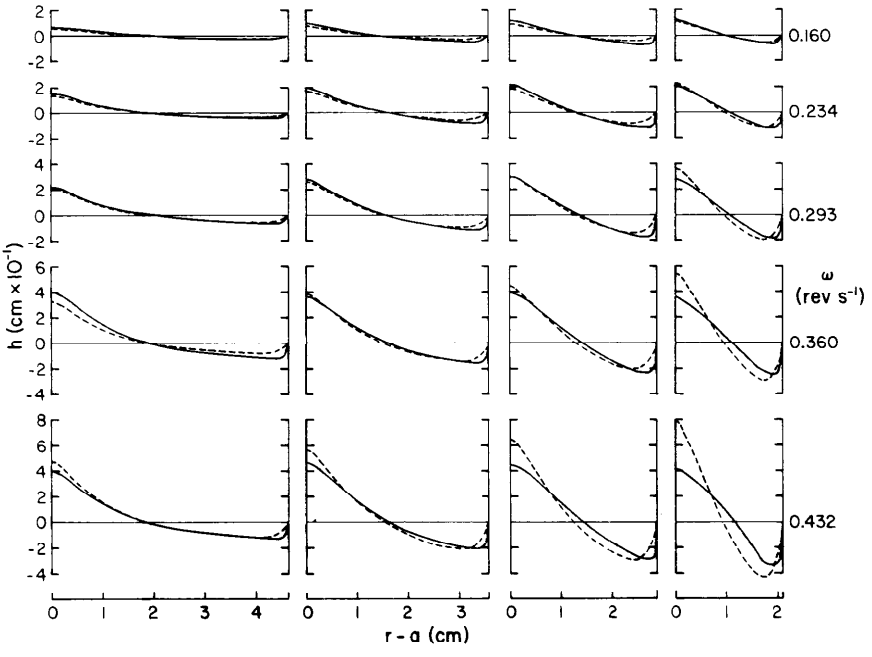

Fig. 19. Experimental (———) and predicted (— — —) profiles for TLA-227 at five different rotational speeds of the inner cylinder. The radius of the outer cylinder is 8.588 cm, and the radii of the four inner cylinders are 3.936, 5.018, 5.704 and 6.477 cm.

in the experiments. The agreement between measured and predicted profiles is good at the lower angular velocities, and gets progressively worse as the angular velocity is increased, when effects of higher order than second begin to dominate.

The free surface on a viscoelastic fluid with a much smaller value of the climbing constant than that of TLA-227 can assume an interesting variety of shapes which are very sensitive to the radii of the cylinders. The free surface shapes on the STP sample used for Fig. 1 are shown in Fig. 20 for several values of the inner cylinder radius. Predicted profiles for two values of the climbing constant have been plotted in order to emphasize once more the influence that relatively small changes in temperature can have on free surface experiments. For example, Fig. 2 shows that the two values of $\hat{\beta}$ used for Fig. 20 correspond to a temperature change of about 5°C. It is clear from the large differences in the pairs of profiles shown in Fig. 20 that changes in temperature of only 1°C could have a marked effect on the free surface shape.

Experimentally-measured profiles are compared with predicted profiles in Fig. 21. The agreement between measured and predicted profiles at the lowest rotational speeds is again good, except for the largest inner cylinder (smallest gap size) where the lowest rotational speed may already be beyond the region of applicability of the second order theory. We attribute some of the smaller

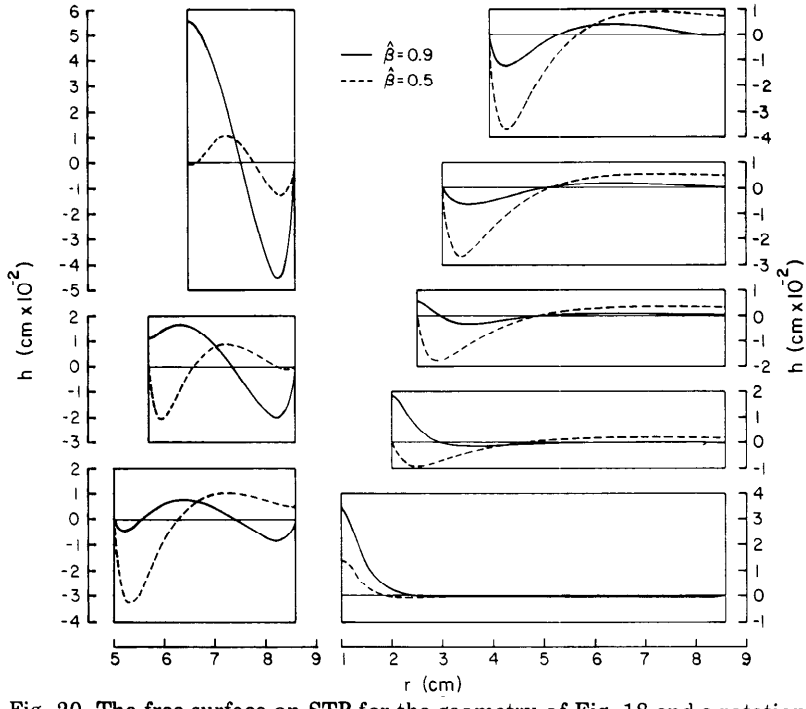

Fig. 20. The free surface on STP for the geometry of Fig. 18 and a rotational speed of 1.00 rev s^{-1}. Profiles for $\hat{\beta}$ = 0.9 and 0.5 are given. The maximum climb is not always at the inner cylinder.

discrepancies between measured and predicted profiles at the lower rotational rates to possible non-uniformities in the fluid temperature. We can infer from Fig. 1 that the second-order region extends to higher rotational speeds for STP than it does for TLA-227, and we found it necessary to run at higher rotational speeds in order to produce measurable displacements. The higher rotational speeds lead to small perturbations in fluid temperature. We think, however, that the comparisons illustrated in Figs. 19 and 21 support the validity of the theoretical predictions at second order, and encourage confidence in the results obtained through order four for the determination of other viscoelastic parameters. Unfortunately, the calculations and experimental procedures required at fourth order are much more elaborate than those at second order and the higher-order theory does not presently seem well suited for rheometrical measurements.

We concluded with a brief remark on the experimental results of Peter and Noetzel [15]. The variation of the climb with radius ratio, demonstrated in Fig. 20 for STP, may help to explain their unexpected, but actually reasonable, results in which they claim to have reduced to zero the height of a climbing fluid in a Couette apparatus by floating the climbing fluid on a bed of mercury. Their Fig. 3 shows that they did not observe climbing of the pyroxy-

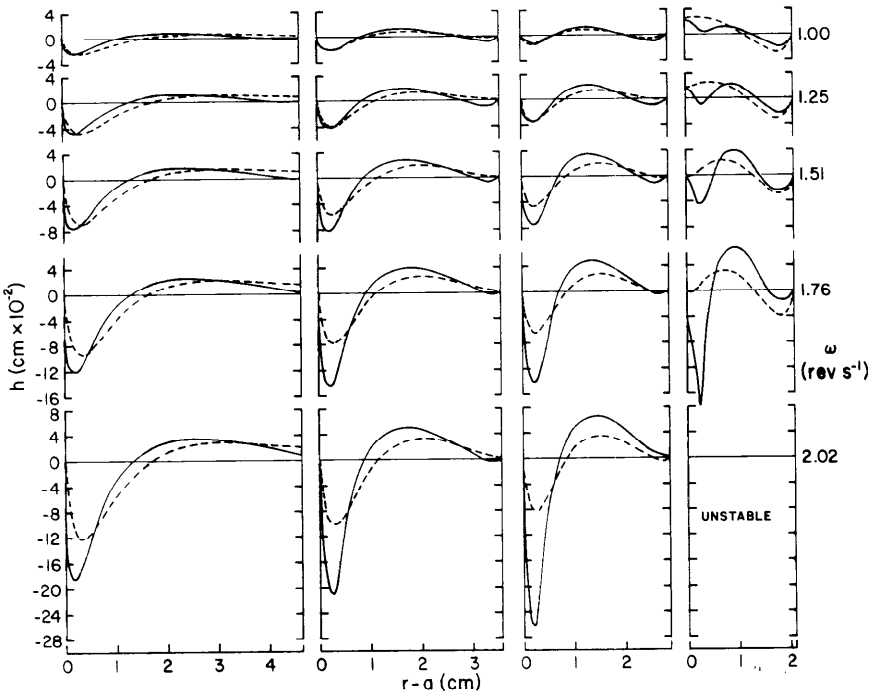

Fig. 21. Experimental (———) and predicted (— — —) profiles for STP for the experimental geometries of Fig. 19.

line solution in butylacetate between concentric cylinders (a = 10.97 cm, b = 16 cm) for various small values of ω. The inner cylinder was situated in a mercury layer at the bottom of the container to produce a state of pure simple shear in the body of the test solution. They interpreted their observations to mean that the Weissenberg effect is either absent or of smaller order in simple shearing flows. Their observation is consistent with our results for STP which show that the climb can be very sensitive to η and also to the size of a, the inner radius. In fact, we compute that there would be an almost negligible rise in height if STP were used in their apparatus at the rotational speeds they employed for their fluid.

Acknowledgements

This work was supported by the U.S. Army Research Office. We gratefully acknowledge the skillful craftsmanship of Mr. Roger Erickson throughout the design and construction of all our experiments, and the invaluable help of Mr. Austris Cers throughout every aspect of all our experimental programs.

References

1 D.D. Joseph and G.S. Beavers, Free surface problems in rheological fluid mechanics, Rheol. Acta, 16 (1977) 169—189.
2 D.D. Joseph and R.L. Fosdick, The free surface on a liquid between cylinders rotating at different speeds: Part I, Arch. Ration. Mech. Anal., 49 (1973) 321—380.
3 D.D. Joseph, G.S. Beavers and R.L. Fosdick, The free surface on a liquid between cylinders rotating at different speeds: Part II, Arch. Ration. Mech. Anal., 49 (1973) 381—401.
4 G.S. Beavers and D.D. Joseph, The rotating rod viscometer, J. Fluid Mech., 69 (3) (1975) 475—511.
5 J.Y. Yoo, Fluid motion between two cylinders rotating at different speeds, Ph.D. Thesis, University of Minnesota, 1977.
6 J.Y. Yoo, D.D. Joseph and G.S. Beavers, Higher order theory of the Weissenberg effect, J. Fluid Mech., (in press).
7 J.M. Dealy and T.K.P. Vu, The Weissenberg effect in molten polymers, J. Non-Newtonian Fluid Mech., 3 (1977/78) 127—140.
8 A.H. Hoffman and W.G. Gottenberg, Determination of the material functions for a simple fluid from a study of the climbing effect, Trans. Soc. Rheol., 17 (1973) 465—485.
9 D.A. Saville and D.W. Thompson, Secondary flows associated with the Weissenberg effect, Nature, 223 (5204) (1969) 391—392.
10 D.D. Joseph and G.S. Beavers, The free surface on a simple fluid between cylinders undergoing torsional oscillations. Part I: Theory. Part II: Experiments, Arch. Ration. Mech. Anal., 62(4) (1976) 323—352.
11 B.E.D. Kolpin, The oscillating rod viscometer, M.S. Thesis, University of Minnesota, 1977.
12 B.E.D. Kolpin, G.S. Beavers and D.D. Joseph, The free surface on a simple fluid between cylinders undergoing torsional oscillations. Part IV: Oscillating rods, (to appear).
13 G.S. Beavers and D.D. Joseph, Novel Weissenberg effects, J. Fluid Mech., 81(2) (1977) 265—272.
14 G.S. Beavers, D.D. Joseph and J.Y. Yoo, The free surface on a liquid between cylinders rotating at different speeds: Part III, (to appear).
15 S. Peter and W. Noetzel, Uber einige Experimente zur Frage der Existenz des Weissenberg-Effektes, Ann. Physik. Chem., 21 (1959) 422—431.
16 G.S. Beavers and D.D. Joseph, Novel Weissenberg Effects, 16 mm Motion Picture.